INORGANIC CHEMISTRY
FRONTIERS

RESEARCH ARTICLE

View Article Online
View Journal | View Issue

Cite this: *Inorg. Chem. Front.*, 2020, **7**, 4118

Improvement in the thermoelectric properties of porous networked Al-doped ZnO nanostructured materials synthesized *via* an alternative interfacial reaction and low-pressure SPS processing†

Raymond V. Rivera Virtudazo,[a,b] Bhuvanesh Srinivasan,[a,c] Quansheng Guo,[a] Rudder Wu,[a] Toshiaki Takei,[a] Yuta Shimasaki,[d] Hiroaki Wada,[d] Kazuyuki Kuroda,[d,e] Slavko Bernik[f] and Takao Mori*[a,g]

Received 22nd July 2020,
Accepted 1st September 2020

DOI: 10.1039/d0qi00888e

rsc.li/frontiers-inorganic

n-Type ZnO-based semiconducting materials are increasingly studied for thermoelectrics (TE) in the past due to their inexpensive and non-toxic nature coupled with their high Seebeck coefficient and stability at elevated temperatures. However, their high thermal conductivity limits their prospect for TE application. In this work, a novel, simpler and faster bottom-up approach to produce thermoelectric Al-doped ZnO ceramics from nanopowders produced by an interfacial reaction (double emulsion method) followed by consolidation by spark plasma sintering (SPS) is explored. This alternative interfacial reaction yielded porous aggregates composed of nanoparticles, which exhibited distinctly enhanced TE performance after densification by SPS at low pressure, due to the notable improvement in the power factor and pronounced suppression of the lattice thermal conductivity caused by the nano/micro-structure engineered by this bottom-up synthesis technique. This encompasses grain size reduction, inclusion of Al-rich nano-precipitates, and nanoporosity, thus enabling scattering of phonons of different mean free paths. A maximum figure of merit ZT ~0.13 at 750 K was obtained for $Zn_{0.97}Al_{0.03}O$ ceramics, a substantial enhancement to the previously reported values for the same composition synthesized by the traditional synthesis methods.

1. Introduction

Thermoelectric (TE) materials with their ability to directly convert waste heat to electrical energy can have the potential to be environmentally friendly and minimize our dependence on fossil-fuel energy.[1–3] The performance of TE materials is generally evaluated by the dimensionless figure of merit, $ZT = S^2T/\rho\kappa = S^2\sigma T/\kappa$, wherein ρ, S, T, and κ are the electrical resistivity (σ is the electrical conductivity), Seebeck coefficient, absolute temperature, and total thermal conductivity, respectively. The total thermal conductivity (κ) is the sum of the contributions from electrons (κ_e) and lattice phonons (κ_{latt}), $\kappa = \kappa_{latt} + \kappa_e$. Hence, the TE efficiency depends on a number of specific material/transport properties. Some of the well-known TE materials for refrigeration and/or power generation are Bi_2Te_3,[4–6] PbTe,[7–9] $Si_{1-x}Ge_x$,[10–12] GeTe,[13–15] *etc.*, wherein their $ZT \geq 1$. However, the drawbacks of using these conventional TE materials are their toxicity, expensive/complicated processing techniques, and poor stability at high temperature or in air.

A potential solution to the challenges faced by the conventional TE materials is to use elementally abundant sulfide,[16–20] silicide[21–24] and oxide[25–29] materials for TE. For high temperature TE applications, stable materials such as borides[30–32] and oxide-based ceramics[25–29,33–37] seem to be promising. Oxide-based materials, which are generally inexpensive, environmen-

[a]*WPI International Center for Materials Nanoarchitechtonics (WPI-MANA), National Institute for Materials Science (NIMS), 1-1 Namiki, Tsukuba 305-0044, Japan. E-mail: MORI.Takao@nims.go.jp; Tel: +81-(0)29-860-4323*
[b]*Department of Material and Resources Engineering & Technology, College of Engineering & Technology, Mindanao State University- Iligan Institute of Technology, Iligan 9200, Philippines*
[c]*CNRS-Saint Gobain-NIMS, UMI 3629, Laboratory for Innovative Key Materials and Structures (LINK), National Institute for Materials Science, 1-1 Namiki, Tsukuba 305-0044, Japan*
[d]*Department of Applied Chemistry, Faculty of Science and Engineering, Waseda University, 3-4-1 Ohkubo, Shinjuku-ku, Tokyo 169-8555, Japan*
[e]*Kagami Memorial Research Institute for Materials Science and Technology, Waseda University, 2-8-26 Nishiwaseda, Shinjuku-ku, Tokyo 169-0051, Japan*
[f]*Department for Nanostructured Materials, Jozef Stefan Institute, 39 Jamova cesta, Ljubljana 1000, Slovenia*
[g]*Graduate School of Pure and Applied Sciences, University of Tsukuba, 1-1-1 Tennoudai, Tsukuba 305-8671, Japan*

†Electronic supplementary information (ESI) available. See DOI: 10.1039/d0qi00888e

tally-friendly and stable at high temperatures, are particularly interesting. However, the synthesis routes for developing such nanostructured p-type and n-type non-toxic oxide TE materials with competitive *ZT* are still complex and quite challenging. Hence, more research efforts are needed in these materials to arrive at a simpler synthesis route. This work is one such attempt aimed at developing such a feasible simpler and efficient route to develop nanostructured oxide-based TE materials.

ZnO, a promising n-type wide bandgap (~3.3 eV) semiconductor with a large Seebeck coefficient (~−400 μV K^{-1}), has been chosen for this work.[28,29,33,38–40] The Zn–O bond has a covalent character because of the small electronegativity difference, which leads to relatively large carrier mobility so that the low charge carrier concentration below 10^{18} cm^{-3} is responsible for the low electrical conductivity.[38] The issue, however, is that the simple wurtzite crystal structure with light Zn and O elements leads to a thermal conductivity >50 W m^{-1} K^{-1} at room temperature.[41–43] The TE properties of ZnO-based ceramics were first reported by Ohtaki[29] and Tsubota.[40] They pioneered Al-doped ZnO because they were particularly interested in their high thermal stability, high electrical conductivity and low toxicity for high-temperature (≥1273 K) TE application. A secondary phase, *i.e.* $ZnAl_2O_4$ (as nanoprecipitates), with intrinsically high resistance, typically appears in Al-doped ZnO ceramics due to the low solubility limit of Al in ZnO.[29,40,44] Though such secondary precipitates slow the electron transport, they are quite effective in suppressing the thermal transport due to the scattering of phonons of selective mean free paths, thus resulting in lower thermal conductivities.[41,45–48] Suppressing κ is an essential requisite for boosting the *ZT* in ZnO-based TE materials. A low resistance n-type Al-doped ZnO bulk material is usually obtained by doping with ~0.5–5 mol% Al_2O_3 followed by sintering at ~1673 K.[28,38] Several attempts and strategies have been adopted in the past with varying degrees of success to reduce the thermal transport in ZnO materials such as doping with homologous compounds like $InO_{1.5}$[49,50] and $GaO_{1.5}$,[39,51] for nanoscale engineering by creating nanoinclusions of planar defects, superstructuring, pores/voids, nano-graining, grain boundaries, point defects, *etc.*[52–60] However, in most cases, the preparation of such ZnO-based nanocomposites involves the laborious process of mechanical alloying (high energy ball milling) or solid-state reactions followed by hot pressing.

In this work, we present a process that would be much simpler and faster compared to the conventional solid-state reaction route for synthesizing nanostructured ZnO-based materials. Herein, the porous ZnO-based powders were synthesized *via* a simple interfacial reaction (double emulsion method) followed by compaction by spark plasma sintering (SPS) at low pressure. This strategic and efficient process resulted in reduced thermal conductivity and a relatively acceptable power factor in ZnO-based materials. The influence of the synthesized starting powder (nanoporous Zn–Al–O, *i.e.*, $NZn_{1-x}Al_xO$) on TE properties of sintered ceramics (T-$NZn_{1-x}Al_xOP$) as a function of Al-content was investigated. The Al-doped ZnO nanostructured ceramics manifested an improved TE performance, thanks to the reduced κ induced by a variety of microstructural features. A maximum, *ZT* ~0.13 at 750 K was obtained for $Zn_{0.97}Al_{0.03}O$ composition, which is comparable with some of the best-reported values at this temperature for Al-doped ZnO ceramics.

2. Materials and methods

2.1. Synthesis

2.1.1. Chemicals/reagents. Ultrapure water (H_2O) was generated using a Milli-Q integral purification system. Aluminum nitrate nonahydrate ($Al(NO_3)_3{\cdot}9H_2O$), zinc nitrate hexahydrate ($Zn(NO_3)_2{\cdot}6H_2O$), hexane (C_6H_{14}, >99%), Tween 80 ($C_{64}H_{124}O_{26}$, M_w ~1310), Span 80 ($C_{24}H_{44}O_6$, M_w ~429, ammonium bicarbonate (NH_4HCO_3, >99%) and ZnO commercial powders (referred as ZnO-Com) were procured from Sigma-Aldrich Company.

2.1.2. $Zn_{1-x}Al_xO$ powder synthesis and compaction by SPS. $Zn_{1-x}Al_xO$ (x = 0.0, 1.0, 2.0 and 3.0 at%) powders were prepared by a double emulsion method at room temperature (Fig. 1).[61–65] Zinc nitrate hexahydrate (26.264 g, Zn $(NO_3)_2{\cdot}6H_2O$, 90.08 mmol) was mixed with aluminum nitrate nonahydrate (0.536 g, $Al(NO_3)_3{\cdot}9H_2O$, 1.429 mmol) and water. The total volume of this water phase (WP1) was fixed to 36 mL, and the mixture was then stirred for at least 8 h. After stirring, the WP1 was immediately poured to an oil phase (OP) consisting of hexane (72 mL), Tween 80 (1.00 g), and Span 80 (0.50 g). The two-phase solution (WP1/OP) was then emulsified (8000 rpm) with a homogenizer for 1 min. After emulsion formation, the mixture was directly poured into an aqueous solution of ammonium bicarbonate (250 mL, 2 mol L^{-1}) with constant stirring for 4 h (water phase 2 (WP2)). The mixture, WP1/OP/WP2, formed a white colloidal solution which was then filtered, washed with deionized water/ethanol, and vacuum dried at 120 °C for 24 h (dried powder, A-$NZn_{1-x}Al_xO$). Then it was calcined at 450 °C for 4 h to remove the excess surfactants (Fig. 1). The calcined powders are referred as $NZn_{1-x}Al_xO$. These powders were then spark plasma sintered (SPS-1080 – SPS Syntex Inc.) in a 10.0 mm diameter graphite die at 950 °C (heating rate of ~100 °C min^{-1}) for ~5 min (holding time) under a low axial force of ~2.2 kN (pressure of ~28 MPa) under an Ar atmosphere (lower than the normal force 2.8 kN). All the sintered samples (referred as T-$NZn_{1-x}Al_xOP$, with the nominal composition for x = 0.0, 1.0, 2.0, and 3.0 at%) had a density of more or less ~90% of the theoretical density. The sintered discs were then cut and polished to the required shapes and dimensions for various TE measurements.

2.2. Measurement of particle and pore size distribution

The particle size distribution (PSD) of the powders was determined using nano-sizer-Delsa instruments (Delsa-NanoC, Beckman Coulter, and Malvern Zetasizer, Malvern Instruments).

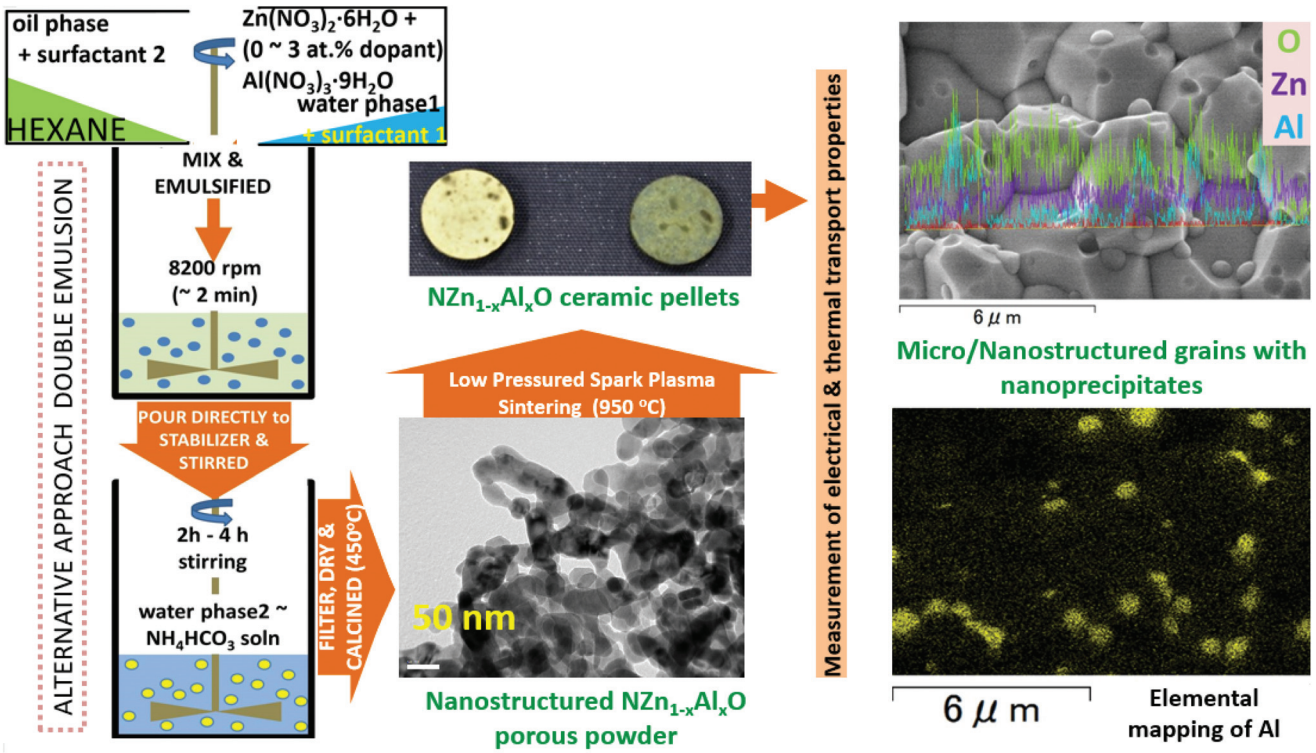

Fig. 1 Schematics of the synthesis of porous networked Al-doped ZnO nanostructured ceramics *via* double emulsion (interfacial reaction) followed by low-pressure-spark plasma sintering.

The surface and pore size distribution were measured using the N_2 sorption method. The pore size distribution was determined by using the Barrett–Joyner–Halenda (BJH) method.[66] The specific surface area ($s.a_{BET}$) was calculated using the Brunauer–Emmett–Teller (BET)[67,68] theory *via* an automatic surface area analyzer (Autosorb iQ_2 Quantachrome instrument) using nitrogen gas (N_2) adsorption and desorption isotherms recorded at 77 K.[69] The total pore volume (V_t) was estimated from the amount adsorbed at a relative pressure of ~0.99. All the dried samples were degassed at 150 °C and 10^{-2} kPa pressure for 22 h prior to the measurement.

2.3. Analysis of structural and micro/nano-structural aspects

The phase composition of the porous powders and sintered ceramic pellets was characterized by X-ray diffraction (XRD, New D8 ADVANCE, Bruker and Ultima3, Rigaku) with Cu-$K_{\alpha 1}$ radiation (λ = 1.54056 Å) at a scanning rate of ~0.02° s^{-1}, an operating voltage of 40 kV and an emission current of 40 mA.

The microstructure of the samples was analyzed by scanning electron microscopy (SEM) and energy-dispersive X-ray spectroscopy (EDX) at a working voltage 10–15 kV using JSM-7001F (JEOL Corp.), S-4800-EDX (Hitachi Corp.) and SU-8000 (Hitachi Corp.) microscopes.

The samples were also investigated using a high-resolution transmission electron microscope (HR-TEM, JEOL JEM 2100F) with a working voltage of 200 kV.

2.4. Measurement of electrical and thermal transport properties

The electrical resistivity (ρ) and Seebeck coefficient (S) were measured simultaneously on bar-shaped samples using a ULVAC-ZEM-2 apparatus.

The thermal diffusivity (D) was measured using a Laser Flash ULVAC-TC7000 instrument. The thermal conductivity (κ) was calculated as a product of thermal diffusivity (D), density, and specific heat (C_p). C_p was measured using a differential scanning calorimeter (DSC, Hitachi HT-Seiko Instrument SII Exstar X-DSC7000, and DSC-8231, Thermo Plus Evo2, Rigaku).

The thermal analysis of the porous powders was performed using an automatic thermogravimetric/differential thermal analyser (TG/DTA, DTG-60, Shimadzu Corp.) with a heating rate of ~10 °C min^{-1}.

The uncertainties in the results for the values of electrical and thermal transport properties were ~5% and ~7%, respectively and the value for the overall ZT was ~12%.

3. Results and discussion

The thermal properties and the minimum calcination temperature to produce the final powders (NZnO and $NZn_{1-x}Al_xO$) were determined from the analysis of the critical weight losses of the as-synthesized A-$Zn_{1-x}Al_xO$ powders by TG/DTA analysis, as shown in Fig. 2(g). Those as-synthesized powders decomposed at ~245–250 °C (~25.2%, peak decomposition) in one

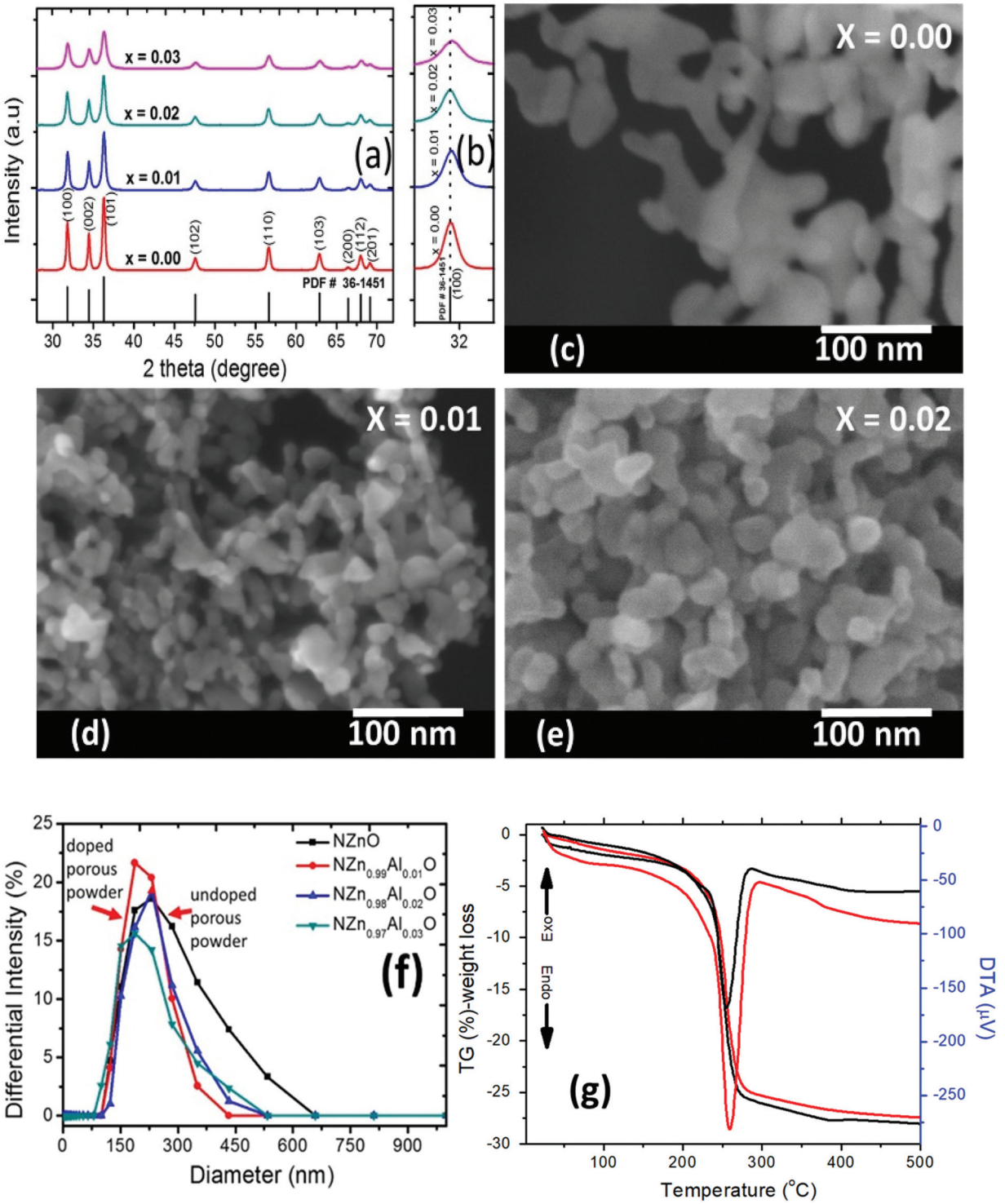

Fig. 2 (a) XRD patterns from 28–75° and (b) a close-up of the (100) reflection between 31 and 33° for the Al-doped ZnO powders. SEM micrographs of $NZn_{1-x}Al_xO$ for x = 0.0 (c), 1.0 (d), and 2.0 at% (e), (f) average particle size distribution of undoped and Al-doped ZnO powders after heat treatment (calcination) at 450 °C in air and (g) TG/DTA profiles of as-synthesized (prepared by the double emulsion method) $Zn_6(CO_3)_2(OH)_6$ (shown in black) and A-$Zn_{0.97}Al_{0.03}O$ (shown in red).

relatively sharp step. The weight-loss, which occurred at ~200–450 °C (~25%), is due to the decomposition of the carbonate groups.[62,70] From these results, the endothermic peak and weight loss can be attributed to de-hydroxylation and decarboxylation.[70,71] Hence, calcination at 450 °C is appropriate to produce the final NZnO and $NZn_{1-x}Al_xO$ powders.

In the XRD pattern of final undoped and Al-doped calcined powders (NZnO and $NZn_{1-x}Al_xO$ powders) shown in Fig. 2(a) and Fig. S1,† the main reflections can be indexed to the hexagonal wurtzite structure of pure ZnO (PDF # 36-1451).[72] Even for the highest Al-content (3 at%), peaks indicating the presence of some Al-containing or other secondary phases cannot be observed from the XRD patterns. Literature reports suggest the thermodynamic solubility limit of Al in ZnO to be lower than 3 at%, with Al^{3+} (r_{ion} ~0.039 nm) being much smaller in size in comparison with Zn^{2+} (r_{ion} ~0.06 nm).[73–75] The double emulsion (interfacial reaction) method, a non-equilibrium process,[76] might have enabled the incorporation of additional content of dopants than permitted by the thermodynamic limit. Such similar phenomena have been found in other out-of-equilibrium processes such as chemical vapor synthesis (CVS)[44] and hybrid flash-SPS processing.[77–79] The peak broadening along (100) reflection with the increase in Al-concentration, as depicted in Fig. 2(b) and Fig. S1†, indicates the decrease in the crystallite size of the particles with Al-content, which is not surprising given the size difference between Zn^{2+} and Al^{3+}. This variation in the crystallite sizes with Al-content has also been confirmed from the microscopic studies (this will be elaborated further in the forthcoming section). Since Al has a smaller ionic radius than Zn, it could be expected that its successful incorporation into the wurtzite ZnO structure on Zn sites would cause a unit-cell shrinkage and a shift of the peaks to higher 2θ values. However, this is not evident/observed from the XRD. The possibility is that the excess Al is finely segregated on the surface or in the surface region of the ZnO nanoparticles as a thin amorphous or poorly crystalline Al–O layer, and hence it might not be detected by XRD.[80] Such a layer can influence the decrease of the crystallite size; however, it would be very difficult to detect it even by TEM analysis.

The morphology of the calcined powders (NZnO and $NZn_{1-x}Al_xO$) is depicted in the SEM images (Fig. 2(c)–(e) and Fig. S2†), which indicates that the powders are basically composed of porous aggregates of the nanoparticles. The PSD data shown in Fig. 2(f) estimate a broader size distribution for these aggregated nanocrystals, which are smaller compared to those of commercial ZnO powder. The aggregation of these nanoparticles has led to the formation of porous networked nanostructured materials (NZnO and $NZn_{1-x}Al_xO$). To confirm the porosity of NZnO and $NZn_{1-x}Al_xO$ samples, N_2 adsorption–desorption isotherms at 77 K using the BET method for the surface area ($s.a_{BET}$) and the BJH method for pore-size distribution (PD) were analyzed, as shown in Fig. 3 (the inset shows PD). The specific surface area ($s.a_{BET}$) of undoped NZnO powders was ~70 $m^2\ g^{-1}$ and the pore volume (V_{BJH}) was ~0.20 $cm^3\ g^{-1}$. The surface area of all the samples is almost in

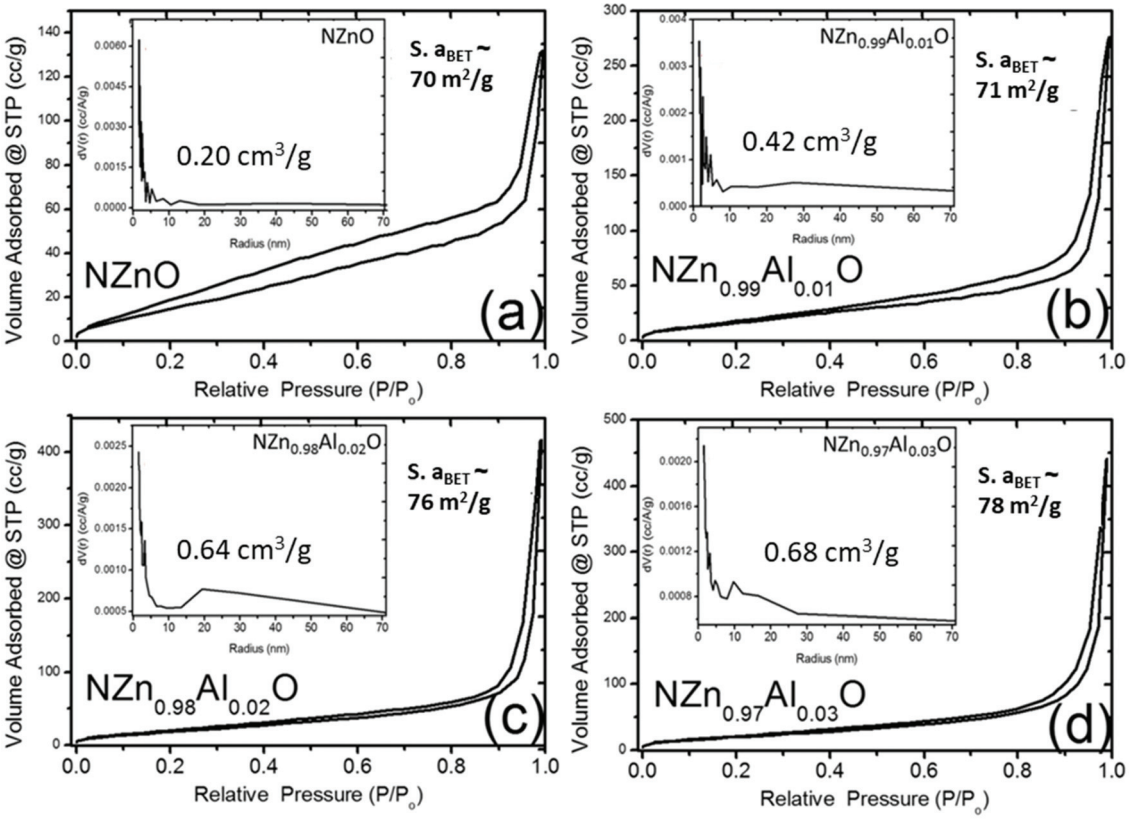

Fig. 3 Nitrogen adsorption–desorption isotherms (a–d) of $NZn_{1-x}Al_xO$ powders (with the nominal composition for x = 0.0, 1.0, 2.0, and 3.0 at% of Al, respectively) after heat treatment at 450 °C in air. The inset shows the corresponding BJH (Barrett–Joyner–Halenda) pore size distribution.

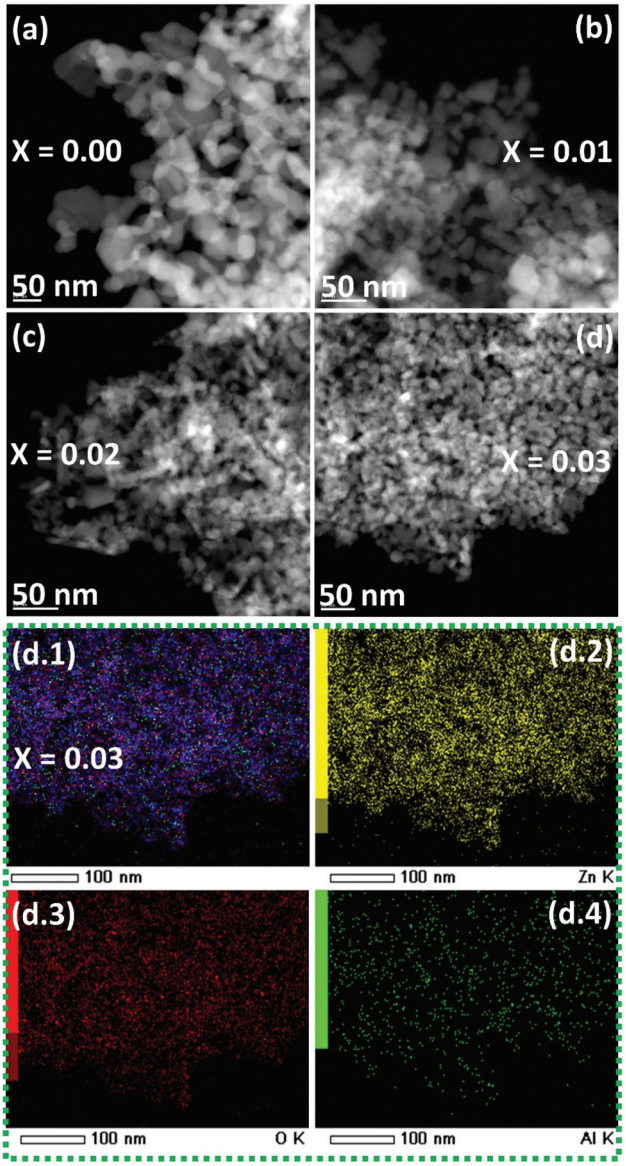

Fig. 4 TEM micrographs (a–d) of $NZn_{1-x}Al_xO$ (with the nominal composition for x = 0.0, 1.0, 2.0, and 3.0 at% of Al, respectively), TEM-EDX chemical mapping (d.1–d.4) for $NZn_{0.97}Al_{0.03}O$ after heat treatment at 450 °C in air.

the same range from 70–80 $m^2\ g^{-1}$. These synthesized samples (NZnO and $NZn_{1-x}Al_xO$) exhibit higher $s.a_{BET}$ than the commercial ZnO powder, suggesting that the creation of the porous network comes from the effect of the interparticle space generated from the self-aggregation of the individual nanoparticles.[62,63,81]

TEM (Fig. 4) and HRTEM (Fig. 5) images confirm the porous nature of the nanostructured materials. The TEM-EDX mapping (Fig. 4(d.1)–(d.4) and Fig. S3†) reveals a homogeneous distribution of Al in the ZnO matrix. The enlarged HRTEM images of the $NZn_{0.97}Al_{0.03}O$ sample (Fig. 5(e) and (f)) show parallel and clear lattice fringes, with lattice spacings ~0.271 nm and ~0.2833 nm along (002) and (100) planes of the hexagonal ZnO phase. The neatly arranged spots as rows/arrays in the FFT pattern (as shown in the inset in Fig. 5(f)) can be ascribed to the wurtzite (ZnO) structure.

The XRD pattern of the SPS processed/sintered samples (T-NZnOP and T-$NZn_{1-x}Al_xOP$) can be indexed to the hexagonal wurtzite phase of ZnO (PDF # 36-1451),[72,82,83] as shown in Fig. 6. However, at a higher Al-content ($x \geq 0.02$), some minor secondary reflections corresponding to the gahnite phase *i.e.* $ZnAl_2O_4$ (PDF # 77-732)[84,85] are also present, as depicted in the enlarged image in Fig. 6(e). The proportion of these secondary phases in these sintered materials increases with Al-content. SEM micrographs with EDX mapping (Fig. 7 and Fig. S4–S9†) clearly show that these secondary phases exist as nanoprecipitates (tiny globules distributed homogeneously across the grains of the ZnO aggregates/matrix). This secondary $ZnAl_2O_4$ phase, which is believed to be formed by the reaction of ZnO + Al_2O_3, was also observed in other literature reports when they SPS sintered Al-doped ZnO materials at higher temperatures.[86] Looking at the SEM images from the fractured surface of the sintered materials (Fig. 8), it is quite evident that the grain size decreases systematically and becomes finer with the increase in Al-content. It seems like Al-doping restrains the mobility of the grain boundaries in accordance with the Zener pinning effect by the formation of the nano-scale precipitates of $ZnAl_2O_4$ at grain boundaries during the sintering process, which results in suppressed grain growth. Solid-state micro/nano-structural transformations, such as grain growth or precipitation, involve the motion of the grain boundaries, which is a product of the driving pressure (*i.e.* resultant of the energy stored in the microstructure) and the grain boundary mobility.[87] Repression of the grain boundary mobility with Al-doping can enable the pores to linger to the moving grain boundaries during the sintering process.[88,89]

The temperature-dependent electrical resistivities for the sintered samples are presented in Fig. 9(a). The sintered samples exhibited low, metallic-type electrical resistivity. In all cases, the electrical resistivity increased with temperature, suggesting the degenerated semiconducting behavior in these Al-doped ZnO materials. The undoped ZnO possessed high resistivity, which decreased considerably with Al-doping due to the substitution of aliovalent Al^{3+} for Zn^{2+}, which resulted in higher charge carrier density. There is no clear trend of the electrical transport properties as a function of Al-content. This could be due to reasons such as the possibility of the secondary spinel phase leading to some cationic/anionic imbalance in ZnO with some O deficiency. Though the changes in the trend with electrical transport properties seem to be due to the role of the contribution of secondary (spinel) phases in these materials, it is difficult to quantify and coherently correlate for each composition. The 3 at% Al-doped ZnO sample exhibited the lowest electrical resistivity of $\sim 2.3 \times 10^{-6}\ \Omega$ m ($\sigma \sim 4.4 \times 10^5$ S m^{-1}) at RT, and it increased to $\sim 3.73 \times 10^{-6}\ \Omega$ m ($\sigma \sim 2.7 \times 10^5$ S m^{-1}) at 750 K. It is worth noting that the electrical resistivity of the undoped ZnO (T-NZnOP) prepared by this double emulsion method is much lower than that of the commercial ZnO sample (Fig. S10†), despite both being consolidated

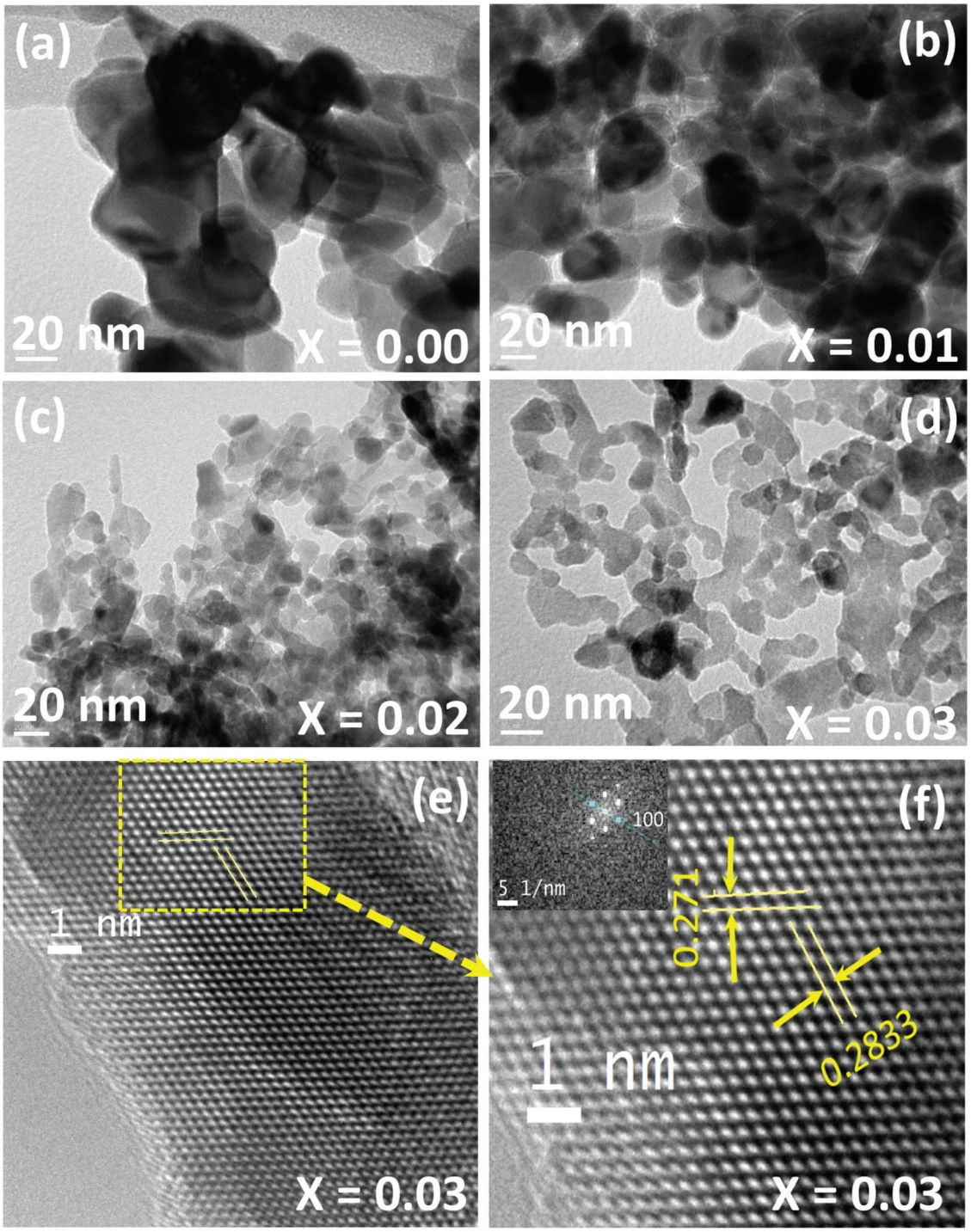

Fig. 5 TEM micrographs – (a–d) $NZn_{1-x}Al_xO$ powders (with the nominal composition for x = 0.0, 1.0, 2.0, and 3.0 at% of Al) after heat treatment at 450 °C in air, HR-TEM images – (e and f) $NZn_{0.97}Al_{0.03}O$ powders with the FFT pattern in the inset of (f).

under the same sintering conditions. The electrical conductivity of these sintered samples (T-NZnOP and T-$NZn_{1-x}Al_xOP$) that were synthesized from fine, porous-networked powders is found to be superior to what was reported in the literature for the same compositions that were prepared by other different synthesis routes.[44,54,55,57,58,82,83,90] This difference is more pronounced when these values of electrical resistivity of our sintered (under an Ar atmosphere) samples are compared with the other literature reports of ZnO-based ceramics that were sintered in air.[29,40,56,91] It is known that the sintering of ZnO in air can result in intrinsic acceptor states, *i.e.*, zinc vacancies (V_{Zn}) and oxygen interstitials (O_i), at the grain boundaries and

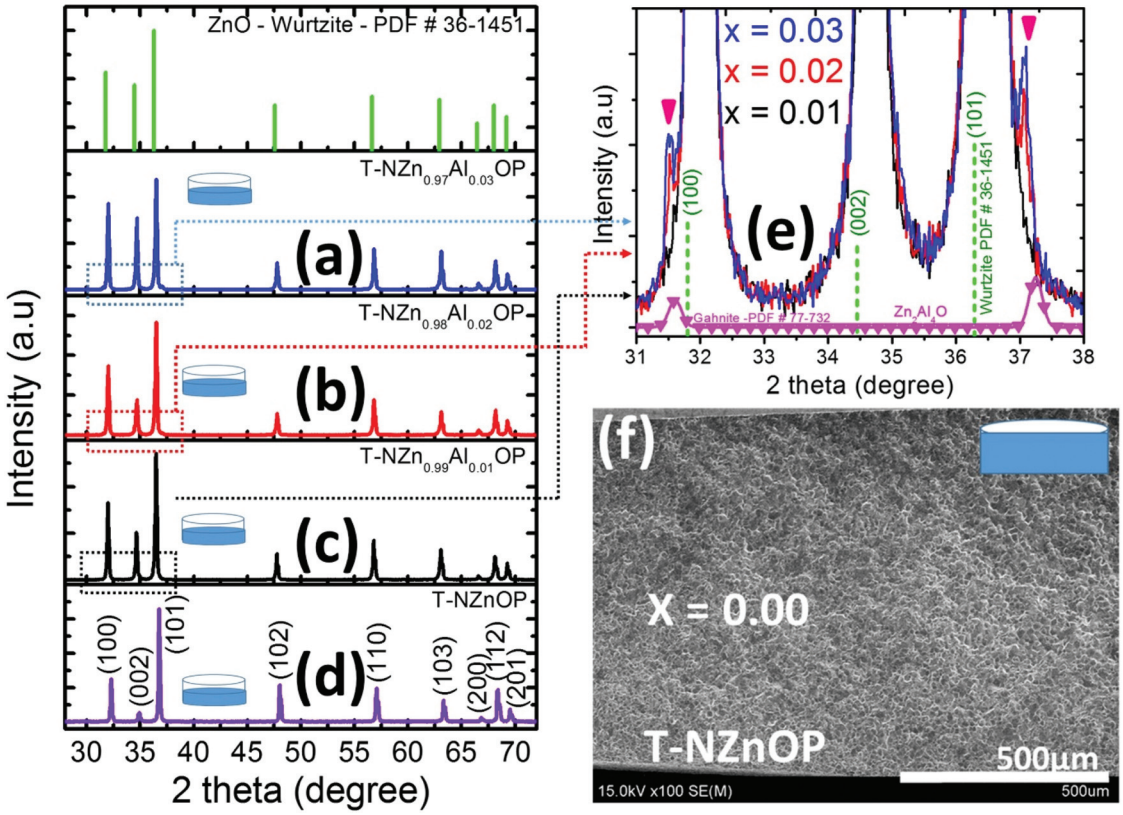

Fig. 6 XRD patterns of sintered T-$NZn_{1-x}Al_xOP$ with the nominal composition for x = 0.0, 1.0, 2.0, and 3.0 at% of Al (a–d) samples, (e) enlarged/zoomed-in vision of the XRD pattern showing the reflections for the $ZnAl_2O_4$ phase, and (f) the cross-sectional SEM micrograph of T-NZnOP.

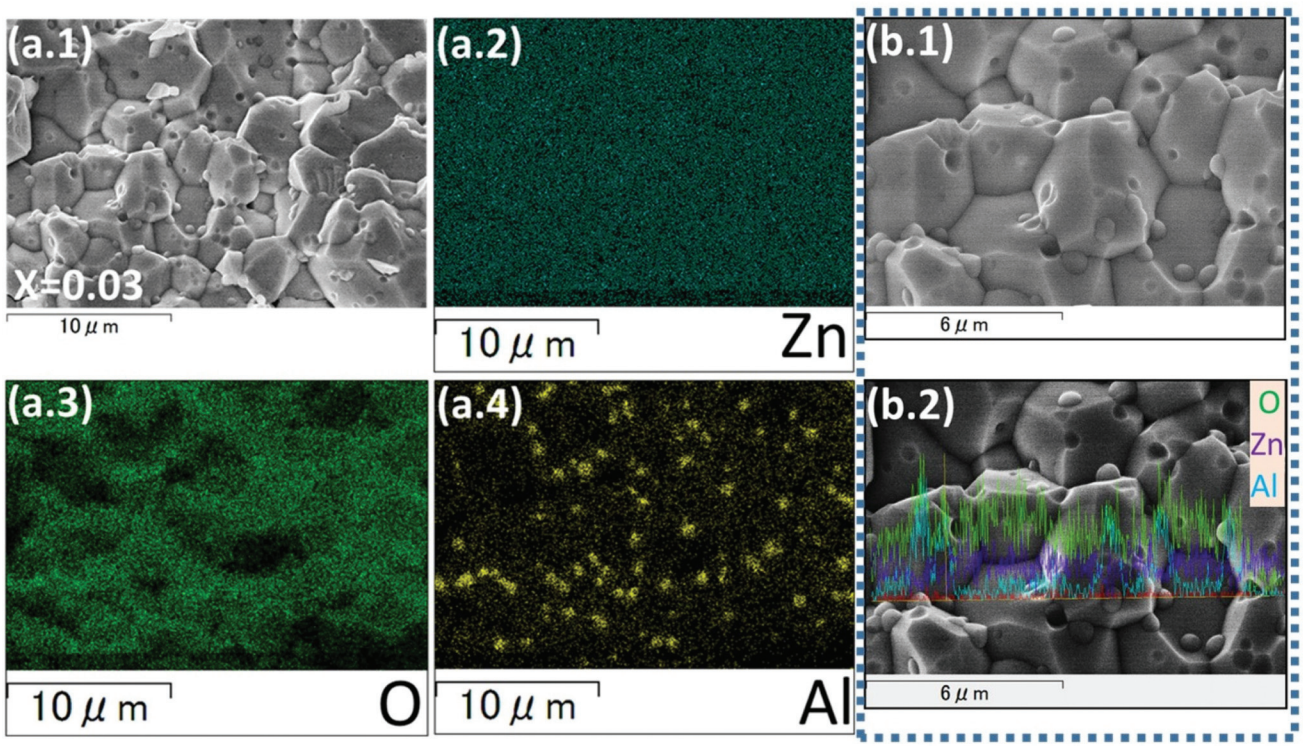

Fig. 7 SEM (a.1, b.1) and EDX chemical mapping images [(a.2) for Zn, (a.3) for O, and (a.4) for Al] for the sintered T-$NZn_{0.97}Al_{0.03}OP$ sample. $ZnAl_2O_4$ precipitates, mapped by yellow (in a.4), are homogeneously distributed along the grain boundaries of the ZnO matrix. (b.2) EDX line scan for elemental O, Zn and Al.

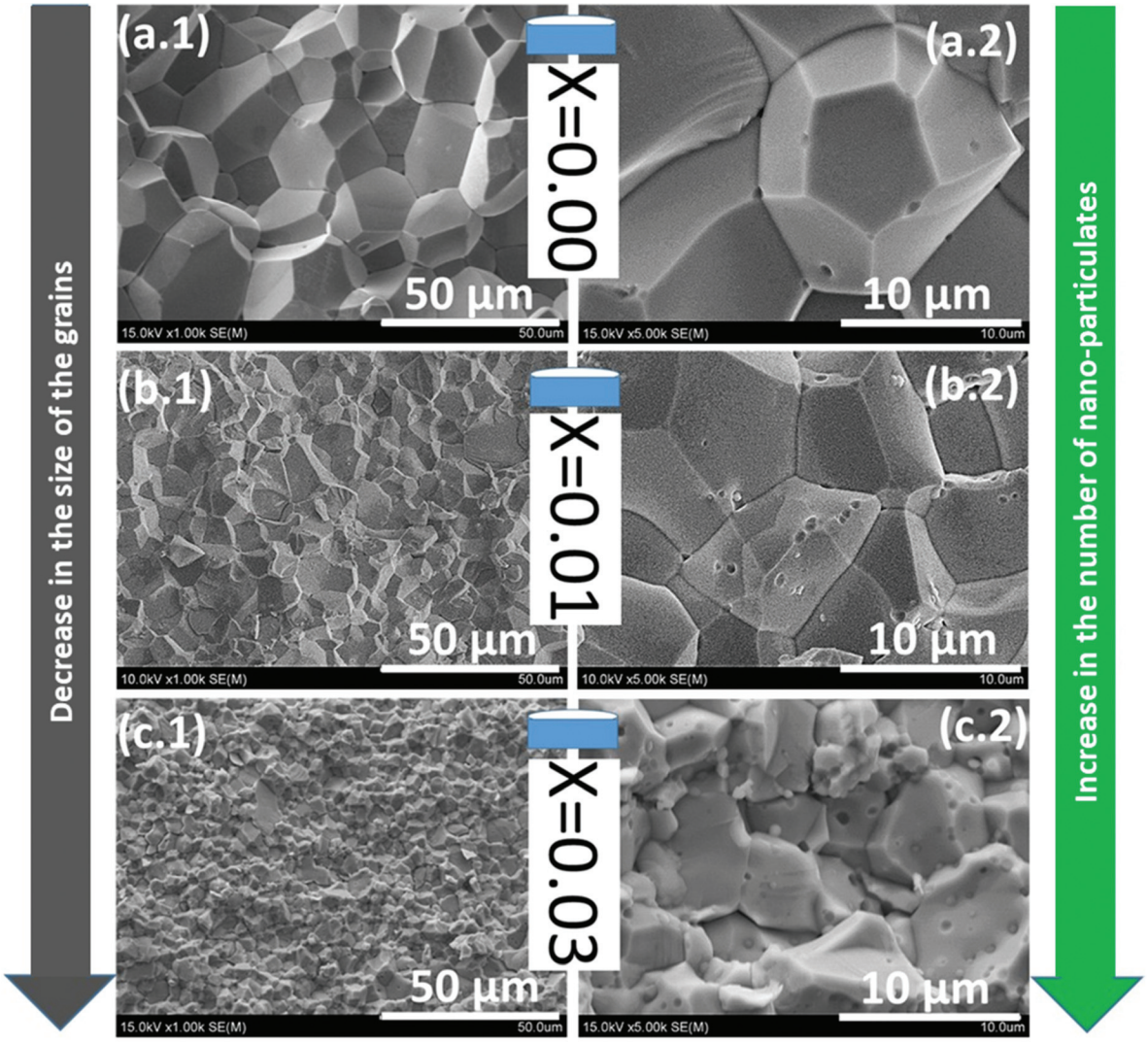

Fig. 8 Cross-sectional SEM micrographs of sintered T-$NZn_{1-x}Al_xOP$ (x = 0.0–0.03) samples [with the nominal composition for x = (a.1, a.2) 0.00, (b.1, b.2) 0.01, (c.1, c.2) 0.03], showing a systematic reduction in grain size with Al-content and the presence of $ZnAl_2O_4$ precipitates (these precipitates are chemically mapped in Fig. 7).

hence the formation of electrostatic Schottky barriers at the grain boundaries with a breakdown voltage of ~0.1 V and higher, which can markedly increase the resistivity of the ceramics.[92,93] It was also reported recently that the classical sintering of ZnO ceramics under an inert atmosphere (N_2) and especially a reducing atmosphere (N_2 + CO mixture) reduces or completely eliminates the formation of the intrinsic acceptor states at the grain boundaries.[94] A further study also confirmed those results, with the elimination of acceptor V_{Zn} and O_i states at the grain boundaries, when the ZnO-based ceramics were SPS processed under vacuum,[95] just like the case under an inert/N_2 + CO atmosphere.

The temperature-dependent Seebeck coefficients of the sintered samples are presented in Fig. 9(b). The negative values of S across the whole temperature range for all the samples confirm the n-type nature of the semiconductor, *i.e.*, electrons as majority charge carriers. The absolute value of S for all samples increased with temperature. The undoped ZnO sample exhibited the highest Seebeck coefficient, and it subsided with the Al-content. This is expected, as Al-doping increased the charge carrier density in ZnO, thus resulting in a reduction in S (and increase in σ). The extraordinary improvement in σ for these samples prepared by interfacial reactions followed by SPS also means that their S-values are bound to be on a lower side when compared with commercial ZnO and other ZnO-based materials that were produced by different synthesis methods.

The temperature-dependent thermoelectric power factor (PF = S^2/ρ or $S^2\sigma$) for the sintered samples is presented in Fig. 10(b). All the samples T-$NZn_{1-x}Al_xOP$ (with the nominal composition for x = 0, 0.01, 0.02, 0.03) prepared from the nanostructured porous ZnO powders exhibited high values of

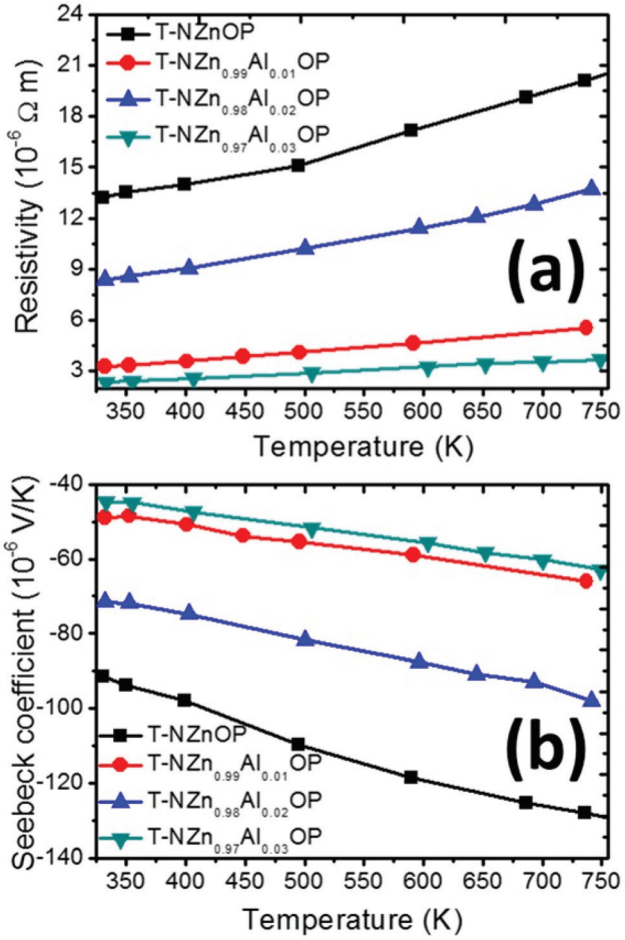

Fig. 9 Temperature-dependent (a) electrical resistivity and (b) Seebeck coefficient for sintered T-NZn$_{1-x}$Al$_x$OP (with the nominal composition for x = 0.0, 1.0, 2.0, and 3.0 at% of Al) samples.

PF. The values of the PF for the undoped ZnO that are reported here (in the range from 6.34 × 10^{-4} W m^{-1} K^{-2} at 325 K to 8.17 × 10^{-4} W m^{-1} K^{-2} at 750 K) are some of the highest for the pristine ZnO. For comparison, the values of PF for the commercial ZnO prepared by this technique were much lower (in the range of 1.75 × 10^{-4} W m^{-1} K^{-2} at 325 K to 0.68 × 10^{-4} W m^{-1} K^{-2} at 750 K), despite a high S (Fig. S10 and S11†). The highest values of PF are manifested by the T-NZn$_{0.97}$Al$_{0.03}$OP sample (in the range of 8.45 × 10^{-4} W m^{-1} K^{-2} at 325 K to 10.70 × 10^{-4} W m^{-1} K^{-2} at 750 K), which are likely among or almost equivalent with the highest values of PF reported for Al-doped ZnO ceramics.[54,60,90,96] The reduction in S-values is compensated by the exceptional increase in σ, thus resulting in strikingly high PF in these porous networked Al-doped ZnO ceramics.

The temperature-dependent total thermal conductivity (κ) of the sintered samples is presented in Fig. 10(a), which shows a decreasing trend with temperature. The undoped ZnO sample exhibited high κ (~40 W m^{-1} K^{-1} at 325 K), and with the addition of Al, κ values decreased substantially. The differences in the values of κ were much smaller at elevated temperatures, *i.e.*, ~8 W m^{-1} K^{-1} for the undoped ZnO sample and ~4 W m^{-1} K^{-1} for the 2 at% Al-doped ZnO sample. As elaborated in the introductory section, κ constitutes contribution from both electrons and lattice phonons. Considering that the addition of Al has resulted in increased electrical conductivity, κ_e is bound to increase proportionately, and in spite of this increase in κ_e with the addition of Al, the total thermal conductivity has significantly been reduced, implying the remarkable suppression of the lattice contribution (κ_{latt}) with the addition of Al to ZnO. This is more astonishing when compared with the commercial ZnO, whose σ is few orders of magnitude lower than our T-NZn$_{1-x}$Al$_x$OP (x = 0, 0.01, 0.02, 0.03) samples (and hence lower κ_e), yet the commercial ZnO only exhibited comparable (if not, relatively higher) κ when compared with our sintered samples. This clearly demonstrates the potential of our novel synthesis method (interfacial reaction/double emulsion method to produce ZnO-based porous-networked agglomerates, which were then consolidated by SPS processing) to markedly suppress the phononic contribution to the thermal conductivity in ZnO-based ceramics. Factors such as interfaces among nanoparticles, particle size, the density of the sintered body and lattice distortion induced by the dopant can affect thermal conductivity, especially the lattice contribution to the thermal conductivity, as the heat-carrying phonons of different mean free paths (MFP) can be scattered when they collide with such precipitates, defects, and interfaces. In this case, the reduction in κ_{latt} can be attributed to the systematic reduction in the grain size with the addition of Al (as depicted in Fig. 7), as reducing the grain-size is known to enhance the boundary scattering of heat-carrying phonons in the inter-grain region.[46,55,57,77] The porous network between these aggregates also plays a crucial role in the reduction of κ_{latt}, as observed in several other cases, including the earlier reported nanoporous ZnO-based materials.[44,54,58,82,97,98] It must be noted that the density of the undoped, 1%, 2%, 3 at% Al-doped sintered materials was, respectively, found to be 89%, 94%, 97%, and 93% of their theoretical density. Moreover, the presence/inclusion of $ZnAl_2O_4$ nano-precipitates that were homogenously distributed along the grain boundaries during the sintering process also plays a key role in the reduction of thermal conductivity, as these precipitates can hinder the transport or scatter the phonons of medium-wavelength MFP (between 10 and 100 nm).[99] However, for such an arbitrary nanostructured material (like ZnO in this case), it would be difficult and tedious to estimate the phonon-boundary scattering rates, which are usually obtained from the Casimir limit and other related scattering mechanisms by using the Matthiessen rule.[100,101] The values of the thermal conductivity obtained here are as low as the values obtained by other out-of-equilibrium processes such as the chemical vapor synthesis (CVS)[44] technique, and comparable with the values that were reported by M. Ohtaki *et al.*[29,40,58] for Al-doped ZnO materials. To put succinctly, this novel synthesis route has resulted in grain size reduction, inclusions ($ZnAl_2O_4$ nano-precipitates), and nanoporosity, all of which can scatter a wide spectrum of phonons (long, mid and short-wavelength

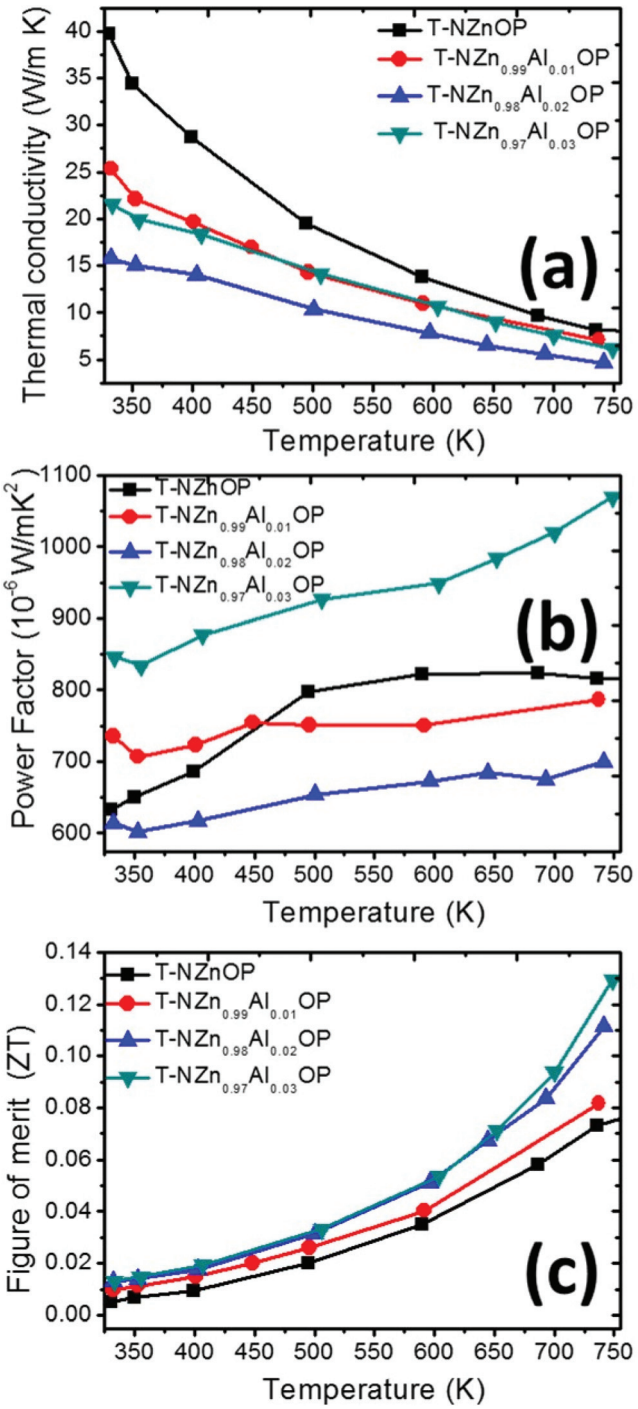

Fig. 10 Temperature-dependent (a) thermal conductivity, (b) power factor, and (c) figure of merit for sintered T-$NZn_{1-x}Al_xOP$ (with the nominal composition for x = 0.0, 1.0, 2.0, and 3.0 at% of Al) samples.

phonons) depending on the sizes of these features, thus enabling achieving a multi-scale hierarchical architecture, *i.e.*, a panoscopic approach[8,99,102] to effectively suppress κ_{latt} in these T-$NZn_{1-x}Al_xOP$ (x = 0, 0.01, 0.02, 0.03) ceramics.

The temperature-dependent thermoelectric figure of merit (ZT) for the sintered samples is presented in Fig. 10(c). The cumulative effect of the markedly improved power factor and significantly suppressed thermal transport for these porous networked T-$NZn_{1-x}Al_xOP$ (with the nominal composition for x = 0, 0.01, 0.02, 0.03) ceramics prepared by an alternative interfacial reaction and SPS processing has resulted in a notable improvement in their ZT. The undoped ZnO (T-NZnOP) exhibited ZT_{max} ~0.075 at 750 K, which is much greater than that of the usual commercial ZnO (ZT_{max} ~0.005 at 750 K, Fig. S11†) and the ZT values coherently increased with Al-content. 3 at% Al-doped ZnO (T-$NZn_{0.97}Al_{0.03}OP$) manifested the highest ZT_{max} ~0.13 at 750 K, which is comparable with most of the best-reported values for this composition.[29,40,44,59,82,90] and on a par with few of the best-reported ZT values for a similar composition.[56]

There is still some scope for further improvement in the TE performance of these ZnO-based ceramics, with better optimization of synthesis and processing conditions. Moving forward, this simpler and faster alternative interfacial reaction (double emulsion method) followed by SPS processing can potentially be used as a strategic synthesis methodology for producing highly efficient TE ceramics.

4. Conclusion

Al-doped ZnO ceramics (T-$NZn_{1-x}Al_xOP$, with x = 0–0.03) were synthesized *via* an easy, faster, and economic interfacial reaction (double emulsion method) followed by compaction by SPS processing. The porous networked aggregates obtained by the interfacial reaction, when sintered by the SPS process, exhibited a notably improved thermoelectric performance. The improved TE performance was due to the cumulative integration of significantly improved electrical conductivity and strikingly reduced lattice thermal conductivity. The suppressed thermal transport was due to the manipulated nano/microstructure engineering, made feasible by this bottom-up synthesis technique. This synthesis route along with the aliovalent donor dopant action of Al^{3+} in ZnO has not only resulted in increased carrier concentration (and hence increased electrical conductivity), but has also more importantly resulted in the reduction of grain growth, and inclusion of $ZnAl_2O_4$ nano-precipitates, thus enabling achieving towards the 'all-scale hierarchical architecture' for producing materials with suppressed thermal transport and enhanced TE performance. ZT_{max} ~0.13 at 750 K for 3 at% Al-doped ZnO and ZT_{max} ~0.075 at 750 K for the undoped ZnO produced by this simple and efficient synthesis methodology exceed the values for most of the earlier reported materials of the same composition that were synthesized by other traditional synthesis routes.

Conflicts of interest

There are no conflicts to declare.

Acknowledgements

This research work was supported by JSPS JP19H00833, JP19F19720, JP16H06441, JP17H02749, and JST Mirai JPMJMI19A1, CREST JPMJCR19Q4. B. S. thanks JSPS for the postdoctoral fellowship (P19720) and Dr David Berthebaud (CNRS) for the constant support. R. V. R. V. thanks Dr Leila Rubia (De Montfort University, UK) and Ms Christine Celeste Chua-Nakar for their help and Mr Makito Nakatsu and Dr Hidehiko Tanaka from NIMS for the technical support.

References

1 D. M. Rowe, *Thermoelectrics Handbook: Macro to Nano*, ed. D. M. Rowe, CRC Press, Boca Raton, FL, 2006, ch. 1.
2 J. He and T. M. Tritt, Advances in Thermoelectric Materials Research: Looking Back and Moving Forward, *Science*, 2017, **357**, eaak9997.
3 I. Petsagkourakis, K. Tybrandt, X. Crispin, I. Ohkubo, N. Satoh and T. Mori, Thermoelectric Materials and Applications for Energy Harvesting Power Generation, *Sci. Technol. Adv. Mater.*, 2018, **19**, 836–862.
4 D. A. Wright, Thermoelectric Properties of Bismuth Telluride and Its Alloys, *Nature*, 1958, **181**, 834–834.
5 H. J. Goldsmid, Bismuth Telluride and Its Alloys as Materials for Thermoelectric Generation, *Materials*, 2014, **7**, 2577–2592.
6 B. Poudel, Q. Hao, Y. Ma, Y. Lan, A. Minnich, B. Yu, X. Yan, D. Wang, A. Muto, D. Vashaee, X. Chen, J. Liu, M. S. Dresselhaus, G. Chen and Z. Ren, High-Thermoelectric Performance of Nanostructured Bismuth Antimony Telluride Bulk Alloys, *Science*, 2008, **320**, 634–638.
7 Y. Pei, X. Shi, A. LaLonde, H. Wang, L. Chen and G. J. Snyder, Convergence of Electronic Bands for High Performance Bulk Thermoelectrics, *Nature*, 2011, **473**, 66–69.
8 K. Biswas, J. He, I. D. Blum, C.-I. Wu, T. P. Hogan, D. N. Seidman, V. P. Dravid and M. G. Kanatzidis, High-Performance Bulk Thermoelectrics with All-Scale Hierarchical Architectures, *Nature*, 2012, **489**, 414–418.
9 A. D. LaLonde, Y. Pei and G. J. Snyder, Reevaluation of $PbTe_{1-x}I_x$ as High Performance N-Type Thermoelectric Material, *Energy Environ. Sci.*, 2011, **4**, 2090–2096.
10 G. Joshi, H. Lee, Y. Lan, X. Wang, G. Zhu, D. Wang, R. W. Gould, D. C. Cuff, M. Y. Tang, M. S. Dresselhaus, G. Chen and Z. Ren, Enhanced Thermoelectric Figure-of-Merit in Nanostructured p-Type Silicon Germanium Bulk Alloys, *Nano Lett.*, 2008, **8**, 4670–4674.
11 X. W. Wang, H. Lee, Y. C. Lan, G. H. Zhu, G. Joshi, D. Z. Wang, J. Yang, A. J. Muto, M. Y. Tang, J. Klatsky, S. Song, M. S. Dresselhaus, G. Chen and Z. F. Ren, Enhanced Thermoelectric Figure of Merit in Nanostructured N-Type Silicon Germanium Bulk Alloy, *Appl. Phys. Lett.*, 2008, **93**, 193121.
12 N. Mingo, D. Hauser, N. P. Kobayashi, M. Plissonnier and A. Shakouri, "Nanoparticle-in-Alloy" Approach to Efficient Thermoelectrics: Silicides in SiGe, *Nano Lett.*, 2009, **9**, 711–715.
13 S. Perumal, S. Roychowdhury and K. Biswas, High Performance Thermoelectric Materials and Devices Based on GeTe, *J. Mater. Chem. C*, 2016, **4**, 7520–7536.
14 J. Li, X. Zhang, Z. Chen, S. Lin, W. Li, J. Shen, I. T. Witting, A. Faghaninia, Y. Chen, A. Jain, L. Chen, G. J. Snyder and Y. Pei, Low-Symmetry Rhombohedral GeTe Thermoelectrics, *Joule*, 2018, **2**, 976–987.
15 J. Shuai, Y. Sun, X. Tan and T. Mori, Manipulating the Ge Vacancies and Ge Precipitates through Cr Doping for Realizing the High-Performance GeTe Thermoelectric Material, *Small*, 2020, **16**, 1906921.
16 C. Bourgès, Y. Bouyrie, A. R. Supka, R. Al Rahal Al Orabi, P. Lemoine, O. I. Lebedev, M. Ohta, K. Suekuni, V. Nassif, V. Hardy, R. Daou, Y. Miyazaki, M. Fornari and E. Guilmeau, High-Performance Thermoelectric Bulk Colusite by Process Controlled Structural Disordering, *J. Am. Chem. Soc.*, 2018, **140**, 2186–2195.
17 Z.-H. Ge, L.-D. Zhao, D. Wu, X. Liu, B.-P. Zhang, J.-F. Li and J. He, Low-Cost, Abundant Binary Sulfides as Promising Thermoelectric Materials, *Mater. Today*, 2016, **19**, 227–239.
18 R. Ang, A. U. Khan, N. Tsujii, K. Takai, R. Nakamura and T. Mori, Thermoelectricity Generation and Electron–Magnon Scattering in a Natural Chalcopyrite Mineral from a Deep-Sea Hydrothermal Vent, *Angew. Chem., Int. Ed.*, 2015, **54**, 12909–12913.
19 K. Suekuni, K. Tsuruta, M. Kunii, H. Nishiate, E. Nishibori, S. Maki, M. Ohta, A. Yamamoto and M. Koyano, High-Performance Thermoelectric Mineral $Cu_{12-x}Ni_xSb_4S_{13}$ Tetrahedrite, *J. Appl. Phys.*, 2013, **113**, 043712.
20 A. U. Khan, R. A. R. A. Orabi, A. Pakdel, J.-B. Vaney, B. Fontaine, R. Gautier, J.-F. Halet, S. Mitani and T. Mori, Sb Doping of Metallic $CuCr_2S_4$ as a Route to Highly Improved Thermoelectric Properties, *Chem. Mater.*, 2017, **29**, 2988–2996.
21 Y. Gelbstein, J. Tunbridge, R. Dixon, M. J. Reece, H. Ning, R. Gilchrist, R. Summers, I. Agote, M. A. Lagos, K. Simpson, C. Rouaud, P. Feulner, S. Rivera, R. Torrecillas, M. Husband, J. Crossley and I. Robinson, Physical, Mechanical, and Structural Properties of Highly Efficient Nanostructured n- and p-Silicides for Practical Thermoelectric Applications, *J. Electron. Mater.*, 2014, **43**, 1703–1711.
22 J. Tani and H. Kido, First-Principles and Experimental Studies of Impurity Doping into Mg_2Si, *Intermetallics*, 2008, **16**, 418–423.
23 H. Ning, G. D. Mastrorillo, S. Grasso, B. Du, T. Mori, C. Hu, Y. Xu, K. Simpson, G. Maizza and M. J. Reece, Enhanced Thermoelectric Performance of Porous Magnesium Tin Silicide Prepared Using Pressure-Less

Spark Plasma Sintering, *J. Mater. Chem. A*, 2015, **3**, 17426–17432.

24 Y. Miyazaki, D. Igarashi, K. Hayashi, T. Kajitani and K. Yubuta, Modulated Crystal Structure of Chimney-Ladder Higher Manganese Silicides $MnSi_{\gamma}$ ($\gamma \sim 1.74$), *Phys. Rev. B: Condens. Matter Mater. Phys.*, 2008, **78**, 214104.

25 I. Terasaki, Y. Sasago and K. Uchinokura, Large Thermoelectric Power in $NaCo_2O_4$, *Phys. Rev. B: Condens. Matter Mater. Phys.*, 1997, **56**, R12685–R12687.

26 H. Ohta, S. Kim, Y. Mune, T. Mizoguchi, K. Nomura, S. Ohta, T. Nomura, Y. Nakanishi, Y. Ikuhara, M. Hirano, H. Hosono and K. Koumoto, Giant Thermoelectric Seebeck Coefficient of a Two-Dimensional Electron Gas in $SrTiO_3$, *Nat. Mater.*, 2007, **6**, 129–134.

27 D. Srivastava, C. Norman, F. Azough, M. C. Schäfer, E. Guilmeau, D. Kepaptsoglou, Q. M. Ramasse, G. Nicotra and R. Freer, Tuning the Thermoelectric Properties of A-Site Deficient $SrTiO_3$ Ceramics by Vacancies and Carrier Concentration, *Phys. Chem. Chem. Phys.*, 2016, **18**, 26475–26486.

28 K. Koumoto, Y. Wang, R. Zhang, A. Kosuga and R. Funahashi, Oxide Thermoelectric Materials: A Nanostructuring Approach, *Annu. Rev. Mater. Res.*, 2010, **40**, 363–394.

29 M. Ohtaki, T. Tsubota, K. Eguchi and H. Arai, High–temperature Thermoelectric Properties of $(Zn_{1-x}Al_x)O$, *J. Appl. Phys.*, 1996, **79**, 1816–1818.

30 T. Mori, Perspectives of High-Temperature Thermoelectric Applications and p-Type and n-Type Aluminoborides, *JOM*, 2016, **68**, 2673–2679.

31 A. Sussardi, T. Tanaka, A. U. Khan, L. Schlapbach and T. Mori, Enhanced Thermoelectric Properties of Samarium Boride, *J. Materiomics*, 2015, **1**, 196–204.

32 T. Mori, Thermoelectric and Magnetic Properties of Rare Earth Borides: Boron Cluster and Layered Compounds, *J. Solid State Chem.*, 2019, **275**, 70–82.

33 K. Koumoto, R. Funahashi, E. Guilmeau, Y. Miyazaki, A. Weidenkaff, Y. Wang and C. Wan, Thermoelectric Ceramics for Energy Harvesting, *J. Am. Ceram. Soc.*, 2013, **96**, 1–23.

34 T. Kajitani, Y. Miyazaki, K. Hayashi, K. Yubuta, X. Y. Huang and W. Koshibae, Thermoelectric Energy Conversion and Ceramic Thermoelectrics, *Mater. Sci. Forum*, 2011, **671**, 1–20.

35 G. Büttner, S. Populoh, W. Xie, M. Trottmann, J. Hertrampf, M. Döbeli, L. Karvonen, S. Yoon, P. Thiel, R. Niewa and A. Weidenkaff, Thermoelectric Properties of $[Ca_2CoO_{3-\delta}][CoO_2]_{1,62}$ as a Function of Co/Ca Defects and Co_3O_4 Inclusions, *J. Appl. Phys.*, 2017, **121**, 215101.

36 R. Daou, R. Frésard, V. Eyert, S. Hébert and A. Maignan, Unconventional Aspects of Electronic Transport in Delafossite Oxides, *Sci. Technol. Adv. Mater.*, 2017, **18**, 919–938.

37 H.-W. Son, Q. Guo, Y. Suzuki, B.-N. Kim and T. Mori, Thermoelectric Properties of $MgTi_2O5$/TiN Conductive Composites Prepared via Reactive Spark Plasma Sintering for High Temperature Functional Applications, *Scr. Mater.*, 2020, **178**, 44–50.

38 E. Guilmeau, P. Díaz-Chao, O. I. Lebedev, A. Rečnik, M. C. Schäfer, F. Delorme, F. Giovannelli, M. Košir and S. Bernik, Inversion Boundaries and Phonon Scattering in Ga:ZnO Thermoelectric Compounds, *Inorg. Chem.*, 2017, **56**, 480–487.

39 Y. Michiue, H. Nishijima, Y. Suzuki and T. Mori, Synthesis and Thermoelectric Properties of Composite Oxides in the Pseudobinary System ZnO-Ga_2O_3, *Solid State Sci.*, 2017, **65**, 29–32.

40 T. Tsubota, M. Ohtaki, K. Eguchi and H. Arai, Thermoelectric Properties of Al-Doped ZnO as a Promising Oxide Material for High-Temperature Thermoelectric Conversion, *J. Mater. Chem.*, 1997, **7**, 85–90.

41 X. Wu, J. Lee, V. Varshney, J. L. Wohlwend, A. K. Roy and T. Luo, Thermal Conductivity of Wurtzite Zinc-Oxide from First-Principles Lattice Dynamics – a Comparative Study with Gallium Nitride, *Sci. Rep.*, 2016, **6**, 1–10.

42 D. I. Florescu, L. G. Mourokh, F. H. Pollak, D. C. Look, G. Cantwell and X. Li, High Spatial Resolution Thermal Conductivity of Bulk ZnO (0001), *J. Appl. Phys.*, 2001, **91**, 890–892.

43 Ü. Özgür, X. Gu, S. Chevtchenko, J. Spradlin, S.-J. Cho, H. Morkoç, F. H. Pollak, H. O. Everitt, B. Nemeth and J. E. Nause, Thermal Conductivity of Bulk ZnO after Different Thermal Treatments, *J. Electron. Mater.*, 2006, **35**, 550–555.

44 D. Gautam, M. Engenhorst, C. Schilling, G. Schierning, R. Schmechel and M. Winterer, Thermoelectric Properties of Pulsed Current Sintered Nanocrystalline Al-Doped ZnO by Chemical Vapour Synthesis, *J. Mater. Chem. A*, 2014, **3**, 189–197.

45 A. U. Khan, K. Kobayashi, D.-M. Tang, Y. Yamauchi, K. Hasegawa, M. Mitome, Y. Xue, B. Jiang, K. Tsuchiya, D. Golberg, Y. Bando and T. Mori, Nano-Micro-Porous Skutterudites with 100% Enhancement in ZT for High Performance Thermoelectricity, *Nano Energy*, 2017, **31**, 152–159.

46 H. Wu, J. Carrete, Z. Zhang, Y. Qu, X. Shen, Z. Wang, L.-D. Zhao and J. He, Strong Enhancement of Phonon Scattering through Nanoscale Grains in Lead Sulfide Thermoelectrics, *NPG Asia Mater.*, 2014, **6**, e108.

47 B. Srinivasan, C. Boussard-Pledel, V. Dorcet, M. Samanta, K. Biswas, R. Lefèvre, F. Gascoin, F. Cheviré, S. Tricot, M. Reece and B. Bureau, Thermoelectric Properties of Highly-Crystallized Ge-Te-Se Glasses Doped with Cu/Bi, *Materials*, 2017, **10**, 328.

48 K. Biswas, J. He, Q. Zhang, G. Wang, C. Uher, V. P. Dravid and M. G. Kanatzidis, Strained Endotaxial Nanostructures with High Thermoelectric Figure of Merit, *Nat. Chem.*, 2011, **3**, 160–166.

49 H. Ohta, W.-S. Seo and K. Koumoto, Thermoelectric Properties of Homologous Compounds in the ZnO–In_2O_3 System, *J. Am. Ceram. Soc.*, 1996, **79**, 2193–2196.

50 H. Kaga, R. Asahi and T. Tani, Thermoelectric Properties of Highly Textured Ca-Doped $(ZnO)MIn_2O_3$ Ceramics, *Jpn. J. Appl. Phys.*, 2004, **43**, 7133.
51 Y. Michiue, T. Mori, A. Prytuliak, Y. Matsushita, M. Tanaka and N. Kimizuka, Electrical, Optical, and Thermoelectric Properties of $Ga_2O_3(ZnO)_9$, *RSC Adv.*, 2011, **1**, 1788–1793.
52 T. Tani, S. Isobe, W.-S. Seo and K. Koumoto, Thermoelectric Properties of Highly Textured $(ZnO)_5In_2O_3$ Ceramics, *J. Mater. Chem.*, 2001, **11**, 2324–2328.
53 N. Vogel-Schäuble, R. Dujardin, A. Weidenkaff and M. H. Aguirre, Influence of Thermal Aging Phenomena on Thermoelectric Properties of Al-Substituted ZnO, *J. Electron. Mater.*, 2012, **41**, 1606–1614.
54 D.-B. Zhang, H.-Z. Li, B.-P. Zhang, D. Liang and M. Xia, Hybrid-Structured ZnO Thermoelectric Materials with High Carrier Mobility and Reduced Thermal Conductivity, *RSC Adv.*, 2017, **7**, 10855–10864.
55 P. Díaz-Chao, F. Giovannelli, O. Lebedev, D. Chateigner, L. Lutterotti, F. Delorme and E. Guilmeau, Textured Al-Doped ZnO Ceramics with Isotropic Grains, *J. Eur. Ceram. Soc.*, 2014, **34**, 4247–4256.
56 X. Qu, W. Wang, S. Lv and D. Jia, Thermoelectric Properties and Electronic Structure of Al-Doped ZnO, *Solid State Commun.*, 2011, **151**, 332–336.
57 Y. Zhao, B. Chen, A. Miner and S. Priya, Low Thermal Conductivity of Al-Doped ZnO with Layered and Correlated Grains, *RSC Adv.*, 2014, **4**, 18370–18377.
58 L. Han, N. V. Nong, W. Zhang, L. T. Hung, T. Holgate, K. Tashiro, M. Ohtaki, N. Pryds and S. Linderoth, Effects of Morphology on the Thermoelectric Properties of Al-Doped ZnO, *RSC Adv.*, 2014, **4**, 12353–12361.
59 P. Jood, R. J. Mehta, Y. Zhang, G. Peleckis, X. Wang, R. W. Siegel, T. Borca-Tasciuc, S. X. Dou and G. Ramanath, Al-Doped Zinc Oxide Nanocomposites with Enhanced Thermoelectric Properties, *Nano Lett.*, 2011, **11**, 4337–4342.
60 P. Jood, R. J. Mehta, Y. Zhang, T. Borca-Tasciuc, S. X. Dou, D. J. Singh and G. Ramanath, Heavy Element Doping for Enhancing Thermoelectric Properties of Nanostructured Zinc Oxide, *RSC Adv.*, 2014, **4**, 6363–6368.
61 T. K. Kim, J. J. Yoon, D. S. Lee and T. G. Park, Gas Foamed Open Porous Biodegradable Polymeric Microspheres, *Biomaterials*, 2006, **27**, 152–159.
62 R. V. R. Virtudazo, M. Fuji and T. Shirai, Fabrication of Calcined Hierarchical Porous Hollow Silicate Micro-Size Spheres via Double Emulsion Process, *Mater. Lett.*, 2011, **65**, 3112–3115.
63 M. Fujiwara, K. Shiokawa, Y. Tanaka and Y. Nakahara, Preparation and Formation Mechanism of Silica Microcapsules (Hollow Sphere) by Water/Oil/Water Interfacial Reaction, *Chem. Mater.*, 2004, **16**, 5420–5426.
64 A. Barhoum, J. Melcher, G. Van Assche, H. Rahier, M. Bechelany, M. Fleisch and D. Bahnemann, Synthesis, Growth Mechanism, and Photocatalytic Activity of Zinc Oxide Nanostructures: Porous Microparticles versus Nonporous Nanoparticles, *J. Mater. Sci.*, 2017, **52**, 2746–2762.
65 R. V. Rivera Virtudazo, Q. Guo, R. Wu, T. Takei and T. Mori, An Alternative, Faster and Simpler Method for the Formation of Hierarchically Porous ZnO Particles and Their Thermoelectric Performance, *RSC Adv.*, 2017, **7**, 31960–31968.
66 E. P. Barrett, L. G. Joyner and P. P. Halenda, The Determination of Pore Volume and Area Distributions in Porous Substances. I. Computations from Nitrogen Isotherms, *J. Am. Chem. Soc.*, 1951, **73**, 373–380.
67 L. D. Gelb and K. E. Gubbins, Characterization of Porous Glasses: Simulation Models, Adsorption Isotherms, and the Brunauer–Emmett–Teller Analysis Method, *Langmuir*, 1998, **14**, 2097–2111.
68 J. J. Freeman and A. I. McLeod, Nitrogen BET Surface Area Measurement as a Fingerprint Method for the Estimation of Pore Volume in Active Carbons, *Fuel*, 1983, **62**, 1090–1091.
69 P. I. Ravikovitch and A. V. Neimark, Characterization of Micro- and Mesoporosity in SBA-15 Materials from Adsorption Data by the NLDFT Method, *J. Phys. Chem. B*, 2001, **105**, 6817–6823.
70 M. Bitenc, M. Marinšek and Z. Crnjak Orel, Preparation and Characterization of Zinc Hydroxide Carbonate and Porous Zinc Oxide Particles, *J. Eur. Ceram. Soc.*, 2008, **28**, 2915–2921.
71 R. Wahab, S. G. Ansari, Y. S. Kim, M. A. Dar and H.-S. Shin, Synthesis and Characterization of Hydrozincite and Its Conversion into Zinc Oxide Nanoparticles, *J. Alloys Compd.*, 2008, **461**, 66–71.
72 K. Kihara and G. Donnay, Anharmonic Thermal Vibrations in ZnO, *Can. Mineral.*, 1985, **23**, 647–654.
73 K. H. Kim, S. H. Shim, K. B. Shim, K. Niihara and J. Hojo, Microstructural and Thermoelectric Characteristics of Zinc Oxide-Based Thermoelectric Materials Fabricated Using a Spark Plasma Sintering Process, *J. Am. Ceram. Soc.*, 2005, **88**, 628–632.
74 M. H. Yoon, S. H. Lee, H. L. Park, H. K. Kim and M. S. Jang, Solid Solubility Limits of Ga and Al in ZnO, *J. Mater. Sci. Lett.*, 2002, **21**, 1703–1704.
75 K. Shirouzu, T. Kawamoto, N. Enomoto and J. Hojo, Dissolution Behavior of Al and Formation Process of $ZnAl_2O_4$ Phases in Al_2O_3-Doped ZnO Sintered Bodies, *Jpn. J. Appl. Phys.*, 2010, **49**, 010201.
76 J. Liu, F. Liu, K. Gao, J. Wu and D. Xue, Recent Developments in the Chemical Synthesis of Inorganic Porous Capsules, *J. Mater. Chem.*, 2009, **19**, 6073–6084.
77 B. Srinivasan, B. Fontaine, F. Gucci, V. Dorcet, T. G. Saunders, M. Yu, F. Cheviré, C. Boussard-Pledel, J.-F. Halet, R. Gautier, M. J. Reece and B. Bureau, Effect of the Processing Route on the Thermoelectric Performance of Nanostructured $CuPb_{18}SbTe_{20}$, *Inorg. Chem.*, 2018, **57**, 12976–12986.
78 B. Srinivasan, A. Gellé, F. Gucci, C. Boussard-Pledel, B. Fontaine, R. Gautier, J.-F. Halet, M. J. Reece and

B. Bureau, Realizing a Stable High Thermoelectric ZT ~ 2 over a Broad Temperature Range in $Ge_{1-x-y}Ga_xSb_yTe$ via Band Engineering and Hybrid Flash-SPS Processing, *Inorg. Chem. Front.*, 2019, **6**, 63–73.

79 F. Gucci, T. G. Saunders, B. Srinivasan, F. Cheviré, D. A. Ferluccio, J.-W. G. Bos and M. J. Reece, Hybrid Flash-SPS of $TiNiCu_{0.05}Sn$ with Reduced Thermal Conductivity, *J. Alloys Compd.*, 2020, 155058.

80 B. Pacewska and M. Keshr, Thermal Transformations of Aluminium Nitrate Hydrate, *Thermochim. Acta*, 2002, **385**, 73–80.

81 Q. Li, E. Liu, Z. Lu, H. Yang and R. Chen, HEPES and Polyol Mediated Solvothermal Synthesis of Hierarchical Porous ZnO Microspheres and Their Improved Photocatalytic Activity, *Mater. Lett.*, 2014, **130**, 115–119.

82 W. H. Nam, Y. S. Lim, S.-M. Choi, W.-S. Seo and J. Y. Lee, High-Temperature Charge Transport and Thermoelectric Properties of a Degenerately Al-Doped ZnO Nanocomposite, *J. Mater. Chem.*, 2012, **22**, 14633–14638.

83 D.-B. Zhang, B.-P. Zhang, D.-S. Ye and Y.-B. Zhu, Thermoelectric Properties of Textured $Zn_{1-x}Al_xO$ Ceramics Prepared by Spark Plasma Sintering of Hydrothermally Synthesized Rod-Shaped Powders, *Ceram. Int.*, 2015, **41**, 14627–14634.

84 S. V. Tsybulya, L. P. Solov'eva, L. M. Plyasova and O. P. Krivoruchko, Complete-Profile Analysis Applied to Nonstoichiometric Spinels, *J. Struct. Chem.*, 1991, **32**, 386–388.

85 S. Mathur, M. Veith, M. Haas, H. Shen, N. Lecerf, V. Huch, S. Hüfner, R. Haberkorn, H. P. Beck and M. Jilavi, Single-Source Sol-Gel Synthesis of Nanocrystalline $ZnAl_2O_4$: Structural and Optical Properties, *J. Am. Ceram. Soc.*, 2001, **84**, 1921–1928.

86 D.-B. Zhang, B.-P. Zhang, P.-P. Shang, C. Gao and Y.-Q. Zhang, Effect of $ZnAl_2O_4$ Phase on Thermoelectric Properties of Al Doped ZnO Ceramics Fabricated by Spark Plasma Sintering, *Mater. Res. Innovations*, 2014, **18**(S4), 110–115.

87 K. G. F. Janssens, D. Olmsted, E. A. Holm, S. M. Foiles, S. J. Plimpton and P. M. Derlet, Computing the Mobility of Grain Boundaries, *Nat. Mater.*, 2006, **5**, 124–127.

88 N. Ma, J.-F. Li, B. P. Zhang, Y. H. Lin, L. R. Ren and G. F. Chen, Microstructure and Thermoelectric Properties of $Zn_{1-x}Al_xO$ Ceramics Fabricated by Spark Plasma Sintering, *J. Phys. Chem. Solids*, 2010, **71**, 1344–1349.

89 K. Park, K. Y. Ko, W.-S. Seo, W.-S. Cho, J.-G. Kim and J. Y. Kim, High-Temperature Thermoelectric Properties of Polycrystalline $Zn_{1-x-y}Al_xTi_yO$ Ceramics, *J. Eur. Ceram. Soc.*, 2007, **27**, 813–817.

90 K. F. Cai, E. Müller, C. Drašar and A. Mrotzek, Preparation and Thermoelectric Properties of Al-Doped ZnO Ceramics, *Mater. Sci. Eng., B*, 2003, **104**, 45–48.

91 J. Hoemke, A. U. Khan, H. Yoshida, T. Mori, E. Tochigi, N. Shibata, Y. Ikuhara and Y. Sakka, Sintering Characteristics and Thermoelectric Properties of Mn–Al Co-Doped ZnO Ceramics, *J. Ceram. Soc. Jpn.*, 2016, **124**, 515–522.

92 A. Janotti and C. G. V. de Walle, Fundamentals of Zinc Oxide as a Semiconductor, *Rep. Prog. Phys.*, 2009, **72**, 126501.

93 K. Ellmer and A. Bikowski, Intrinsic and Extrinsic Doping of ZnO and ZnO Alloys, *J. Phys. D: Appl. Phys.*, 2016, **49**, 413002.

94 T. Tian, L. Cheng, L. Zheng, J. Xing, H. Gu, S. Bernik, H. Zeng, W. Ruan, K. Zhao and G. Li, Defect Engineering for a Markedly Increased Electrical Conductivity and Power Factor in Doped ZnO Ceramic, *Acta Mater.*, 2016, **119**, 136–144.

95 T. Tian, L. Cheng, J. Xing, L. Zheng, Z. Man, D. Hu, S. Bernik, J. Zeng, J. Yang, Y. Liu and G. Li, Effects of Sintering on the Microstructure and Electrical Properties of ZnO-Based Thermoelectric Materials, *Mater. Des.*, 2017, **132**, 479–485.

96 S. Jantrasee, P. Moontragoon and S. Pinitsoontorn, Thermoelectric Properties of Al-Doped ZnO: Experiment and Simulation, *J. Semicond.*, 2016, **37**, 092002.

97 S. Saini, P. Mele, T. Oyake, J. Shiomi, J.-P. Niemelä, M. Karppinen, K. Miyazaki, C. Li, T. Kawaharamura, A. Ichinose and L. Molina-Luna, Porosity-Tuned Thermal Conductivity in Thermoelectric Al-Doped ZnO Thin Films Grown by Mist-Chemical Vapor Deposition, *Thin Solid Films*, 2019, **685**, 180–185.

98 M. Ohtaki and K. Araki, Thermoelectric Properties and Thermopower Enhancement of Al-Doped ZnO with Nanosized Pore Structure, *J. Ceram. Soc. Jpn.*, 2011, **119**, 813–816.

99 L.-D. Zhao, V. P. Dravid and M. G. Kanatzidis, The Panoscopic Approach to High Performance Thermoelectrics, *Energy Environ. Sci.*, 2013, **7**, 251–268.

100 H. B. G. Casimir, Note on the Conduction of Heat in Crystals, *Physica*, 1938, **5**, 495–500.

101 B. Fu, G. Tang and Y. Li, Electron–Phonon Scattering Effect on the Lattice Thermal Conductivity of Silicon Nanostructures, *Phys. Chem. Chem. Phys.*, 2017, **19**, 28517–28526.

102 J. He, M. G. Kanatzidis and V. P. Dravid, High Performance Bulk Thermoelectrics via a Panoscopic Approach, *Mater. Today*, 2013, **16**, 166–176.